



HAL
open science

A Marching Cubes Algorithm: Application for Three-dimensional Surface Reconstruction Based on Endoscope and Optical Fiber

Zhongjie Long, Kouki Nagamune

► **To cite this version:**

Zhongjie Long, Kouki Nagamune. A Marching Cubes Algorithm: Application for Three-dimensional Surface Reconstruction Based on Endoscope and Optical Fiber. *Information*, 2015, 18 (4), pp.1425-1437. hal-01205823

HAL Id: hal-01205823

<https://inria.hal.science/hal-01205823>

Submitted on 28 Sep 2015

HAL is a multi-disciplinary open access archive for the deposit and dissemination of scientific research documents, whether they are published or not. The documents may come from teaching and research institutions in France or abroad, or from public or private research centers.

L'archive ouverte pluridisciplinaire **HAL**, est destinée au dépôt et à la diffusion de documents scientifiques de niveau recherche, publiés ou non, émanant des établissements d'enseignement et de recherche français ou étrangers, des laboratoires publics ou privés.

A Marching Cubes Algorithm: Application for Three-dimensional Surface Reconstruction Based on Endoscope and Optical Fiber

Zhongjie Long^{*,**}, Kouki Nagamune^{*,***}

** Department of Human and Artificial Intelligent Systems, Graduate School of Engineering,
University of Fukui, 3-9-1 Bunkyo, Fukui 910-8507, Japan
E-mail: ryuu@me.his.u-fukui.ac.jp*

*** Key Laboratory of Modern Measurement and Control Technology, Ministry of Education,
Beijing Information Science and Technology University, Beijing 100192, China*

**** Department of Orthopaedic Surgery, Graduate School of Medicine, Kobe University,
7-5-1 Kusunokicho, Chuo-ku, Hyogo, Kobe 650-0017, Japan*

Abstract

In this paper, a marching cubes (MC) algorithm is presented for the three-dimensional (3-D) surface reconstruction based on endoscope images. In general, the classical MC algorithm processes the 3-D medical images obtained from computed tomography (CT) or magnetic resonance (MR), while the volumetric data described in this work are not. Therefore, the purpose of this study mainly focuses on: (1) An active endoscope scanning system that equips an endoscope and optical fiber using for profile measurement of the object, is described in detail; (2) A novel method is also presented to create the regular 3-D grid, which is suitable specifically for the data type of endoscope images. The average errors of the endoscope system on depth detection and surface recover were about 0.50 mm (standard deviation, 0.991) and 2.39 mm (standard deviation, 0.759), respectively. Experimental results on several realistic reconstruction demonstrate the feasibility and good performance of the proposed approach.

Key Words: Surface reconstruction, Marching cubes algorithm, Endoscope

1. Introduction

1.1. Structured light techniques

Structured light techniques aim to recover the profile of an object by applying a unique color coded pattern of light. The basic principle is based on parallax and the use of the geometry of triangles and triangulation, as described in [1]–[3]. In terms of the number of cameras, detection with structured light techniques can be obviously divided into two types, monocular and binocular. Binocular detection, however, needs not to be used while employing structure lighting techniques, since depending only on the trigonometric relationship yielded by the projection device and the imaging sensor, the 3-D position of the source points on the object surface can be computed accurately.

Structured light systems (SLS) have found universal applications for macroscopic detection and depth profiling of objects, mainly because the advantages of speed, accuracy and robustness in 3-D reconstruction of featureless objects (e.g., objects with large smooth surfaces) [4]. For example, an early study reported by Haneishi et al. [5] in 1994, using an endoscope with laser beam projection to measure the profile of a gastrointestinal surface with high precision. As an extension of this technique, an electronic endoscope system [6] consisted of an image fiber and a laser scanner achieved the shape measurement at a high speed with the space-encoding method. Tardif et al. [7] introduced a new method to display undistorted image data directly on the patient to determine the skin surface profiles.

In order to obtain dense and stable 3D acquisition in real cases, a technique that has the advantage of being robust in terms of image processing was proposed by Kawasaki et al. [8], who used only a single-frame image of a grid pattern to achieve dense shape reconstruction that requires. Recently, Achraf et al. [9] developed an active vision system for a medical endoscopy application, where a 3-D cartography of the inspected organ can be reconstructed from a video acquisition using the laser based SLS.

1.2. The MC algorithm

The use of classical MC technique, as originally described by W. Lorensen and H. Cline [10], is probably the most popular approach for extracting isosurfaces from a volumetric dataset [11]. Since the MC technique makes it easier for surgeon to observe and visualize an object in a better sense, it has been applied to many medical applications to overcome the difficulty of imagination related to the complicated anatomical structures of organs or soft tissues. For example, authors [12] proposed a novel and efficient implementation of the MC to reconstruct anatomical structures. An improved MC algorithm reported in [13] was used for modeling the pleural surface of the chest wall.

Commonly, past usage of many volumetric datasets often involved the 2-D cross-sectional “slices” that derived from a CT or MR. These datasets can be segmented and viewed as a stack of intersections with numbers of parallel planes, corresponding to a sequence of 3-D image slices [12]. For each slice, the MC takes it as a regular 3-D grid and each intersection of such a grid is called a voxel. A voxel (volumetric pixel) is a volume element, and a scalar value (voxel content) is associated to it [14]. As illustrated in Fig. 1, one logical cube defined by eight neighboring voxels within adjacent slice S_k and S_{k+1} ($1 < k < n$, where n is the number of slices). Thus, the voxels lay on row x_i ($\forall i$) and column y_i ($\forall i$) of the slice S_k is directly adjacent to the next voxels, which lay on row x_i and column y_i of the slice S_{k-1} and S_{k+1} .

Using a divide-and-conquer approach, the standard MC processes the volumetric dataset cube-by-cube to make up the volume. Given an isovalue, v_{iso} , then the related isosurface can be defined as a function $v_{iso} = v(x, y, z)$ that associates v_{iso} to a set of three-dimensional points (x, y, z) arranged on the edge of each logical cubes. In terms of the isovalue, the volume dataset is divided into two groups, one with $v > v_{iso}$ inside the isosurface itself, and the other with $v < v_{iso}$ outside. Besides, in order to find the isosurface intersection in each cube, the voxels at the eight vertexes of the logical cube are compared against the v_{iso} and an eight bit binary number corresponding to each vertex is generated. The voxels contained in a cube inside the isosurface are associated with 1, while the voxels outside are associated with 0. Based on the eight bit binary number, isosurface intersection algorithm is then performed within each cube.

The exact position of the triangle intersection can be calculated with sub-vertex accuracy by a linear interpolation for each intersected edge. For example, a unit-length edge E^l has end points P_s and P_e , whose scalar values are v_s and v_e , respectively, the position of intersection $I = (I_x, I_y, I_z)$ is then given by the following equation [15]:

$$I_{\{x,y,z\}} = P_{s\{x,y,z\}} + \Delta t(P_{e\{x,y,z\}} - P_{s\{x,y,z\}}) \tag{1.1}$$

where $\Delta t = \frac{v_{iso} - v_s}{v_e - v_s}$.

The last step in original MC is to estimate the gradient vector using finite difference method for each triangle vertex, which is required for calculating the surface normal. Besides, dividing the gradient vector by its length yields the unit normal of the vertex required for the rendering algorithm. At this step, four slices have to be loaded into the memory at one time.

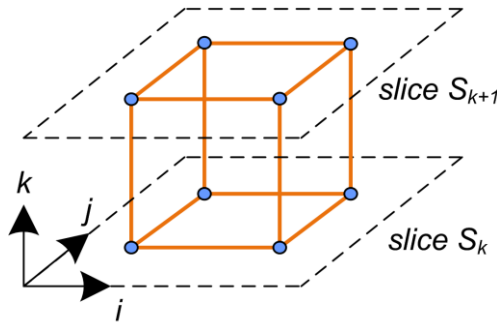


Figure 1. Formation of a logical cube.

1.3. Purpose and organization

As mentioned above, many applications using the MC algorithm involved the CT or MR medical images. In many cases, however, the volumetric dataset are not exactly delivered from the 3-D medical images indeed. For instance, some clinical diagnoses or in-vivo applications, in which endoscopes are employed for observation or shape measurement. Hence, the purpose of this paper is to propose a new method which is suitable specifically for the data type of endoscope images.

The paper is organized as follows. Firstly, the endoscope system is described (Section 2). Then, the proposed MC method, in particular those related to the arrangement of 3-D grid and the surface extraction, are introduced (Section 3). Several sets of experiments are tested and shown in Section 4. Section 5 concludes the paper.

2. Preliminary

2.1. System configuration

The endoscope scanning system is mainly composed of an endoscope and a fiber, as depicted in Fig.2. A lens, one end of the optical fiber, was connected to the projection device of a laser. The laser beam was projected onto the object surface by the fiber tip, the other end of the fiber. Note that the proposed system configuration here differs greatly from the previous study reported in [5] and [6]. That is the endoscope was fixed to the fiber tip with a small tilt angle α (angle between fiber center and the optical axis of camera). In this situation, it is easier and more sensitive to extract the laser beam from the image sequences due to the existence of parallax. The optical fiber and endoscope are shown in Fig. 3. In addition, the diameter of optical fiber is 0.99 mm, while that of endoscope is 7.00 mm.

A calibration for the endoscope scanning system is essential prior to the 3-D measurement experiments. The calibration experiment was carried out with the famous method mentioned in [16]. In this process, several pictures were taken by the endoscope with different view angle and loaded into the project. Then, the internal and extrinsic parameters of the endoscope were obtained, as well as the lens distortion correction parameters.

2.2. Data acquisition

The projection model of the endoscope scanning system is shown in Fig. 4. A point $P_i (\forall i)$ illuminated on the object surface by the laser beam, whose coordinate is (X_i^c, Y_i^c, Z_i^c) , is projected onto the image plane by a ray passing through the projection centre, and its corresponding point on the image plane is p_i . The parameter f is the focal length, while (c_x, c_y) is the principle point. Both of them were given by the output result of the calibration experiment.

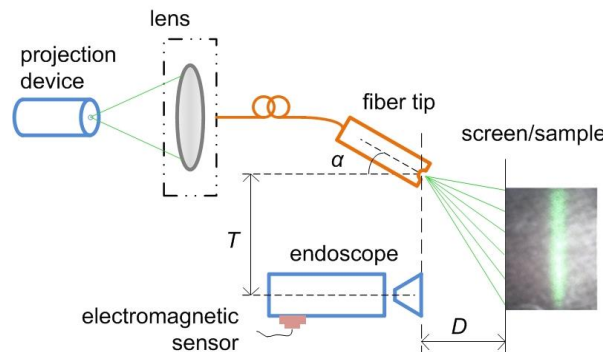


Figure 2. System configuration of endoscope scanning system. T is the distance between the optical axis of camera and the optical fiber tip. D is called scanning gap, along the optical axis from the endoscope tip to the object surface.

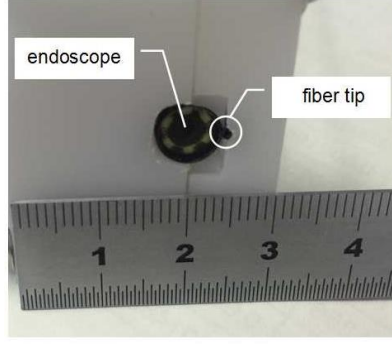


Figure 3. Optical fiber tip and the endoscope

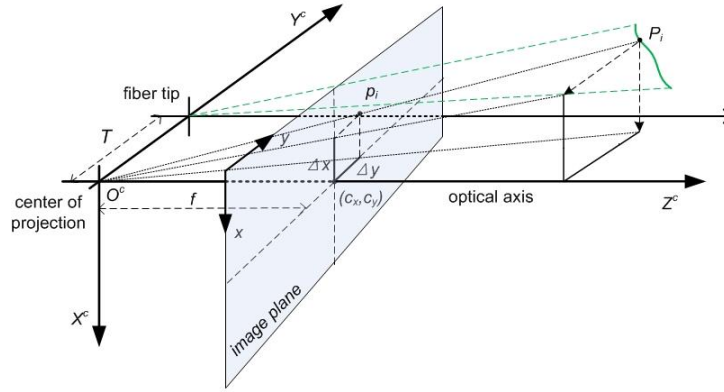


Figure 4. 3-D vision projection model of the endoscope scanning system. The superscript “c” represents that the coordinates being calculated are in the camera coordinate system.

In addition, the 3-D projection model can be decomposed into a 2-D model, as illustrated in Fig. 5. The point p_{i-yz} , projection coordinate of P_i , is yielded when P_i is projected onto the yz -plane. The resulting point y_i on the image plane can be measured in advance, as well as the parameter T and α . Hence, based on the geometry of triangles and triangulation, the 3-D coordinates of points P_i ($\forall i$) illuminated on the object surface can be expressed as:

$$X_{P_i}^c = Z_{P_i}^c (c_x - x_i) / f \quad (2.1)$$

$$Y_{P_i}^c = Z_{P_i}^c (c_y - y_i) / f \quad (2.2)$$

$$Z_{P_i}^c = \frac{Tf}{(c_y - y_i) + f \tan \alpha} \quad (2.3)$$

2.2.1. Electromagnetic sensor

The coordinates of all the spatial points were computed by the use of a six degrees of freedom electromagnetic device (LIBERTY™) manufactured by Polhemus incorporated. The system consists of a transmitter and three sensors. Two of the sensors were fastened to the endoscope and scanning object. The transmitter is the magnetic source and produces the electromagnetic field, which is accurately the reference for the position and orientation measurements for the sensors.

Euler angles of sensors (Fig. 6), including azimuth rotation (ψ), elevation rotation (θ) and roll rotation (ϕ). The tip of the arrow represents the position of the electrical center of the sensor. Therefore, the current position and pose of the sensors with respect to the transmitter state were calculated by applying a rotation matrix R_t and a translation vector t .

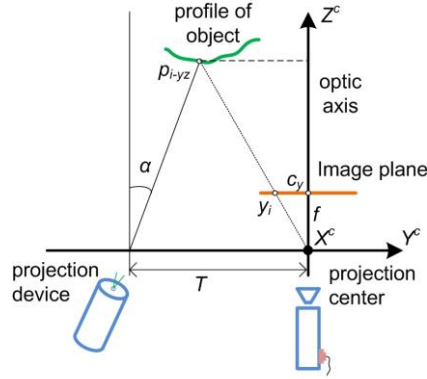


Figure 5. Projection result of a spatial point.

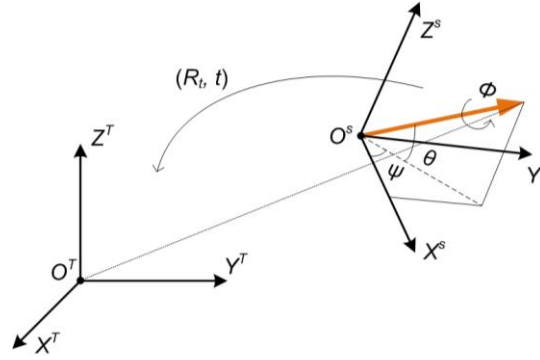


Figure 6. Coordinate conversion from sensor to transmitter coordinate system.

As a result, 3-D coordinates in the transmitter coordinate system of points P_i ($\forall i$) illuminated on the object surface can be derived as follows:

$$\begin{pmatrix} X_{P_i}^T \\ Y_{P_i}^T \\ Z_{P_i}^T \end{pmatrix} = R_z(\psi) R_y(\theta) R_x(\phi) \begin{pmatrix} X_{P_i}^C + L_x \\ Y_{P_i}^C + L_y \\ Z_{P_i}^C + L_z \end{pmatrix} + \begin{pmatrix} X_S^T \\ Y_S^T \\ Z_S^T \end{pmatrix} \quad (2.4)$$

where

$$R_x(\phi) = \begin{pmatrix} 1 & 0 & 0 \\ 0 & \cos \phi & -\sin \phi \\ 0 & \sin \phi & \cos \phi \end{pmatrix}, R_y(\theta) = \begin{pmatrix} \cos \theta & 0 & \sin \theta \\ 0 & 1 & 0 \\ -\sin \theta & 0 & \cos \theta \end{pmatrix}, R_z(\psi) = \begin{pmatrix} \cos \psi & -\sin \psi & 0 \\ \sin \psi & \cos \psi & 0 \\ 0 & 0 & 1 \end{pmatrix},$$

$(L_x, L_y, L_z)^T$ is the relative distance between camera coordinate system and sensor electrical center, and $(X_S^T, Y_S^T, Z_S^T)^T$ is the sensor position relative to the transmitter coordinate system.

3. The proposed MC algorithm

3.1. 3-D grid arrangement

As discussed above, the volumetric dataset can be obtained by the equation (2.4). Nevertheless, the data type or the data structure is not as regular as those of CT and MR. Thus, a novel approach utilizes midpoint comparison to make a 3-D regular grid.

There is only one primary step in our approach to grid arrangement problem. That is a parameter I_c (cube interval) should be set in advance. Parameter I_c determines the size of cubes. For each point located in the cube, three projections along the i, j , or k directions will be calculated respectively. A point is arranged to the coordinate of i, j or k if the projection distance is less than the midpoint on each axis. Otherwise, it is arranged to coordinate $i+1, j+1$ or $k+1$.

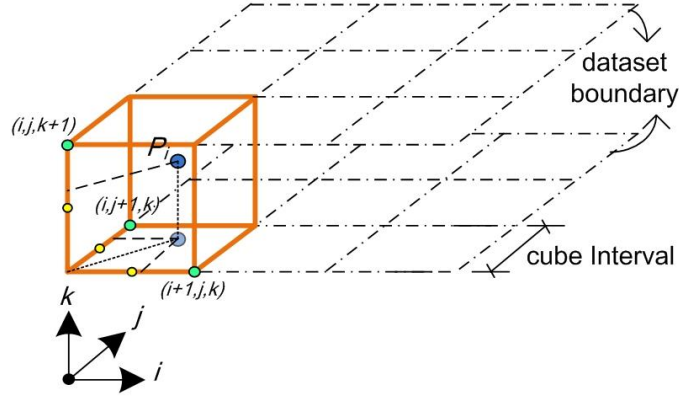


Figure 7. Grid arrangement. Yellow points denote the midpoint of each edge. The vertex will be highlighted if it receives a binary one.

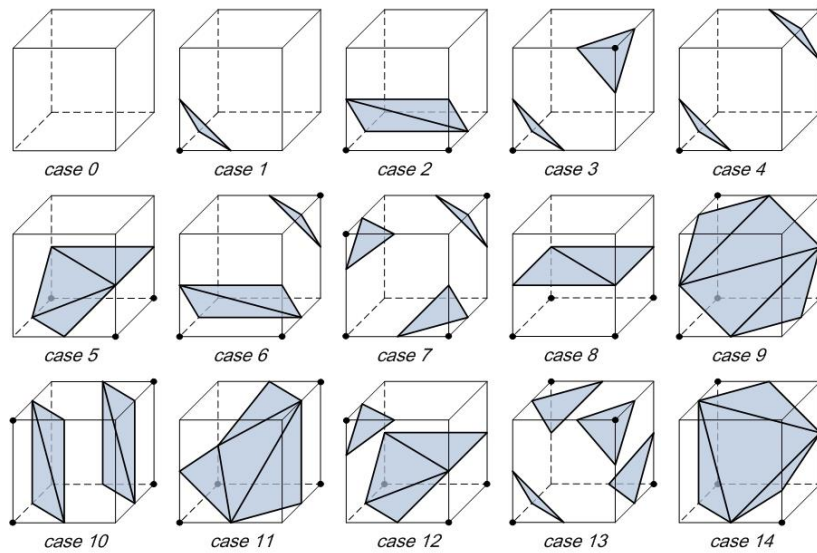


Figure 8. Type of surface combinations for the marching cube algorithm. The black circles means that vertices inside the surface.

As depicted in Fig. 7 , a point P_i among the cube is projected onto the i - j plane. As both the projection distances on i and j axes exceed the midpoint, we assign a binary number 1 to the vertexes $(i+1, j, k)$ and $(i, j+1, k)$ respectively, as well as vertex $(i, j, k+1)$ for the same reason, while the other vertexes in the same cube are set to be binary number 0. Under this assumption, looping on the volumetric dataset derived from the endoscope scanning system, a regular 3-D grid is generated (shown in Fig. 12(c) and Fig. 13(g)). Note that the original volumetric dataset are then replaced by this regular 3-D grid, which is used for surface extraction.

3.2. Surface extraction

The proposed algorithm employs the standard MC look-up table to produce the surface intersection. Taking account of the reflective and rotational symmetries of a cube, the authors [10] reduce all possible combination from 256 cases to 15 basic patterns (shown in Fig. 8).

The simplest pattern, 0, implies that there is no spatial point within the cube at all and thus produces no triangles. The next pattern, 1, implies that only one vertex contained in the cube receives a binary one.

Instead of cell edge linear interpolation, midpoint selection [17], a special method, is utilized to obtained the exactly position of the surface intersection. In contrast with the original MC, midpoint selection does not require any interpolation along with the edge of

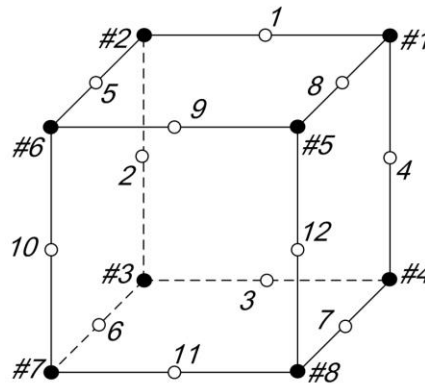


Figure 9. Index for vertex position.

cubes in surface extraction processing. When a cube edge with a binary number, zero or one, the midpoint of the edge is the intersection being looking for.

The midpoints in a cube that can be yielded via midpoint selection are shown in Fig. 9: there are 12 different spatial positions on which triangle vertexes can be intersected. Moreover, an index with eight bit binary number is used to record the vertex position for each logical cube, as shown in Fig. 9 (black circles from #1 to #8). In terms of the eight bit binary number and look-up table, surface extraction can be simply classified and then performed cube-by-cube.

3.3. Surface rendering

Volumetric dataset are often rendered with indirect volume rendering (IVR) technique (such as MC), which involves rendering of an intermediate structure (e.g. an isosurface) that has been extracted from the dataset, typically via automatic means [15]. In contrast, the render method used in our system was OpenGL technique due to the dataset type differs from those of MC.

For the sake of overall computational time, the positions of triangle vertexes intersected on the edge of the cubes were calculated in advance depending on the look-up table. The detailed calculation was saved in a list included in the rendering program.

In summary, the process of the proposed algorithm can be broken down into the following steps:

1. Scan and acquire the dataset from the endoscope system.
2. Set the interval cube parameter to create logical cubes.
3. Yield the regular 3-D grid by comparing the projection distance against the midpoint of cube edges.
4. Obtain the type of surface extraction based on the eight bit binary index.
5. Calculate the positions of surface intersection via midpoint selection method.
6. Render the triangle vertex coordinates.

4. Experimental results

4.1. Precision evaluation

4.1.1. Plane test

Before doing the 3-D reconstruction experiments, it is necessary to investigate the accuracy of this endoscope scanning system. A plane of wood was placed in front of the endoscope at three distances with an interval of 5 mm. Then data collection was carried out while moving the endoscope with a constant scanning gap D . Fig. 10 shows the source data of depth value evaluation.

The laser projection device employed in our system has a property that the best focusing performance occurs only if the scanning gap less than 20 mm. That is why the data of the third group (20 mm) fluctuated mostly. Besides, the laser is rarely extracted from the image plane if the scanning gap less than 8 mm. Although the laser can be extracted successfully, the

average error is similar to the third group. The large error was probably caused by the focal length of the endoscope scanning system being shallow [6], since the laser irradiated from the irradiation face as a flat shape.

As illustrated in Fig. 11, the average error of these data, also we can say the endoscope system, were around 0.50 mm. The standard deviation (SD) of the first group to the third group was 0.503 mm, 0.899 mm and 1.480 mm, respectively. This implies that it is better to choose and control the scanning gap from 10 to 20 mm while scanning the object surface. Fig. 12 shows the recover results of a wood plane.

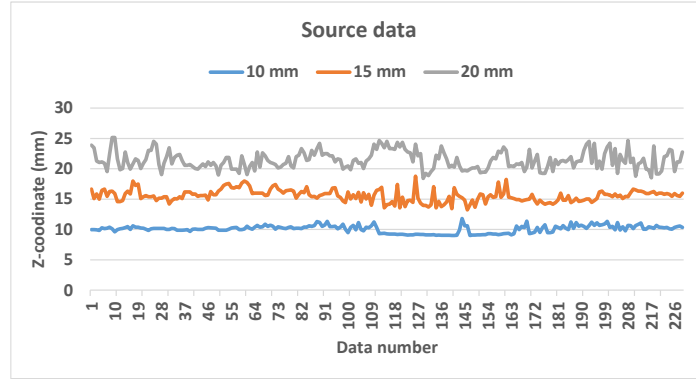


Figure 10. Data acquisition for precision evaluation.

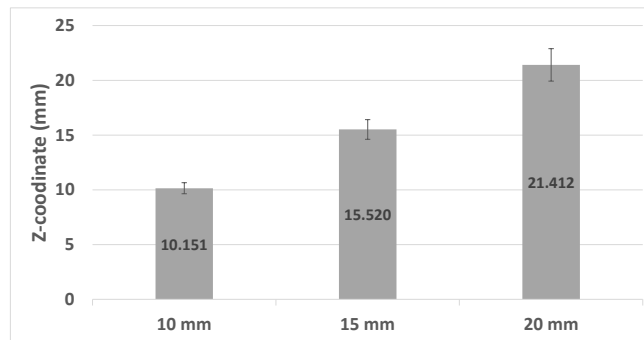


Figure 11. Statistical analysis of the source data.

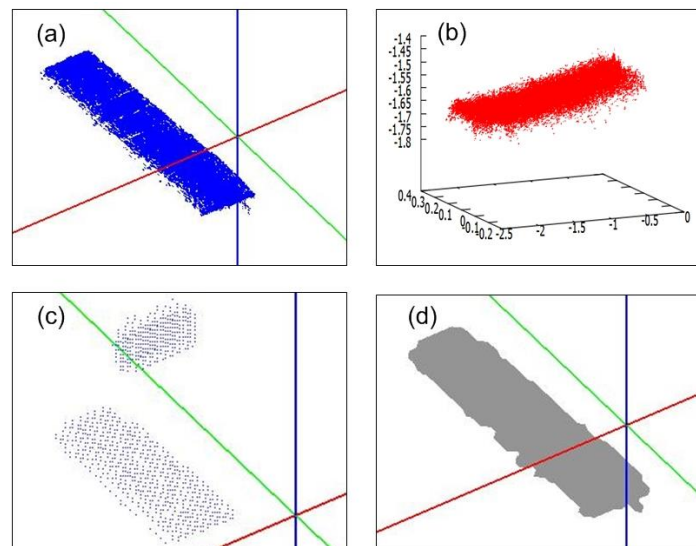


Figure 12. Reconstruction results of a wood plane. (a) Data collection while scanning. (b) Spatial location of all the points. (c) Arrangement of 3-D grid using the proposed MC method. (d) Rendering of the plane with OpenGL techniques.

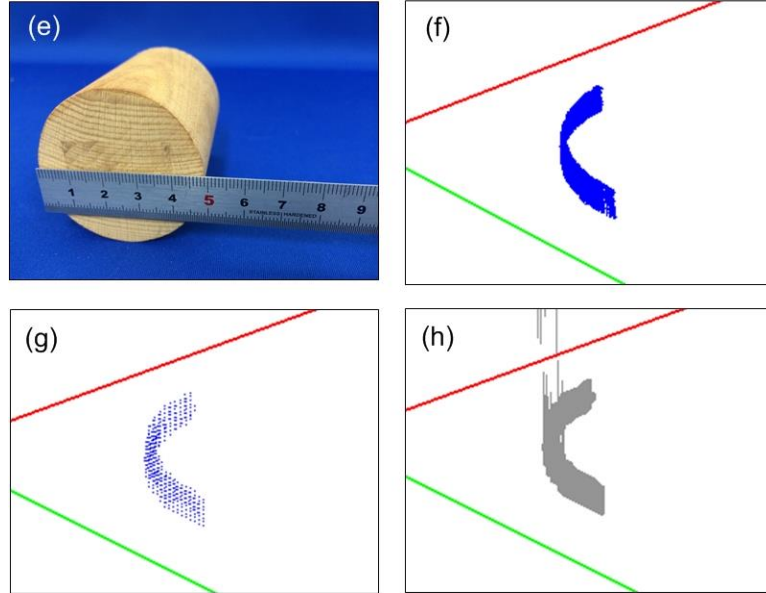


Figure 13. Experimental results of a cylindrical surface. (e) Image of the scanning object. (f) A quarter of the curved surface was scanned. (g) Arrangement effects of the 3-D grid. (h) Surface rendering.

4.1.2. Surface test

A standard cylinder made of wood (49 mm in diameter) was also used for the experiment of precision evaluation. The endoscope was put close to the cylinder and moved along the surface by hands. A quarter of the curved surface was obtained and shown in Fig. 13(f).

To our knowledge, given a series of points (x_i, y_i) , $1 \leq i \leq n$, circles can be represented algebraically by an equation of the form:

$$(x_i - a)^2 + (y_i - b)^2 = r^2 \quad (4.1)$$

or
$$F(a, b, r) = (x_i - a)^2 + (y_i - b)^2 - r^2 \quad (4.2)$$

where (a, b) is the center coordinate and r the radius.

Moreover, if the points distributed in a ring-shape on the xy -plane approximately, we can use the least squares fit (LSF) algorithm [18] to find the equation of the circle that provides a best fit around the data points. That means we should minimize

$$\sum_{i=1}^n F(a, b, r)^2 = \min \quad (4.3)$$

Reading off Eq. (4.3), we obtain

$$\sum_{i=1}^n (x_i^2 + y_i^2 + Ax_i + By_i + C)^2 = \min \quad (4.4)$$

where

$$A = -2a \quad (4.5)$$

$$B = -2b \quad (4.6)$$

$$C = a^2 + b^2 - r^2 \quad (4.7)$$

Let the system of partial differential equations (PDEs) $\partial F / \partial A = 0$, $\partial F / \partial B = 0$, $\partial F / \partial C = 0$, that is

$$\partial F / \partial A = A \sum_{i=1}^n x_i^2 + B \sum_{i=1}^n x_i y_i + C \sum_{i=1}^n x_i + \sum_{i=1}^n x_i^3 + \sum_{i=1}^n x_i y_i^2 = 0 \quad (4.8)$$

$$\partial F / \partial B = A \sum_{i=1}^n x_i y_i + B \sum_{i=1}^n y_i^2 + C \sum_{i=1}^n y_i + \sum_{i=1}^n x_i^2 y_i + \sum_{i=1}^n y_i^3 = 0 \quad (4.9)$$

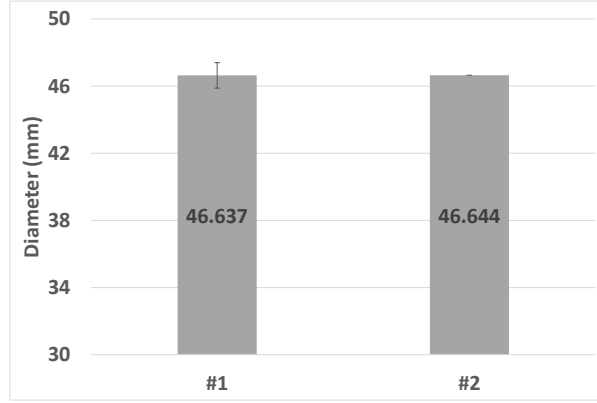


Figure 14. Average diameter of the cylinder surface between source data and LSF.

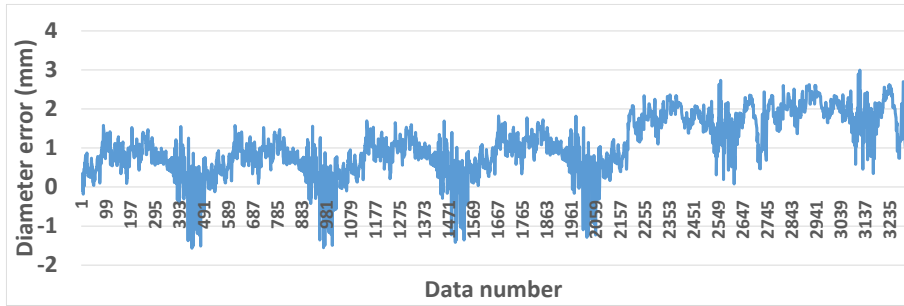


Figure 15. Analysis of diameter error.

$$\frac{\partial F}{\partial C} = A \sum_{i=1}^n x_i + B \sum_{i=1}^n y_i + C \sum_{i=1}^n 1 + \sum_{i=1}^n x_i^2 + \sum_{i=1}^n y_i^2 = 0 \quad (4.10)$$

Eq. (4.8-4.10) can be represented with the matrices form:

$$\begin{pmatrix} \sum_{i=1}^n x_i^2 & \sum_{i=1}^n x_i y_i & \sum_{i=1}^n x_i \\ \sum_{i=1}^n x_i y_i & \sum_{i=1}^n y_i^2 & \sum_{i=1}^n y_i \\ \sum_{i=1}^n x_i & \sum_{i=1}^n y_i & \sum_{i=1}^n 1 \end{pmatrix} \begin{pmatrix} A \\ B \\ C \end{pmatrix} = \begin{pmatrix} -\sum_{i=1}^n (x_i^3 + x_i y_i^2) \\ -\sum_{i=1}^n (x_i^2 y_i + y_i^3) \\ -\sum_{i=1}^n (x_i^2 + y_i^2) \end{pmatrix} \quad (4.11)$$

Solving Eq. (4.11) yields the undetermined coefficients A , B and C . Finally, we can work backwards to solve for a , b and r with Eq. (4.5-4.7).

Hence, basing on the dataset of the quarter curved surface and LSF, we obtained the equation of the circle as below:

$$(x_i - 4.7568)^2 + (y_i + 1.5706)^2 = 23.3221^2 \quad (4.12)$$

The fitting diameter was shown in Fig. 14(#2), while the average diameter of the source data was 46.637 mm (SD, 0.759). Notice that our hypothesis was that the fitting diameter yielded from LSF has a zero SD. Compared with the standard diameter of cylinder, we obtained the diameter error was 2.393 mm, which also represented the error of the endoscope system on the surface reconstruction.

The source dataset had a total point number of 66102. A comparison between the standard diameter and those of fitting was illustrated in Fig. 15. Obviously, the diameter error distributed a series of fluctuation, especially at the beginning of data acquisition. Such a fluctuation were consistent with those mentioned in section 4.1.1. Fig. 16 shows the spatial location of cylinder surface. The center coordinate of the circle calculated using LSF was shown by the arrow.

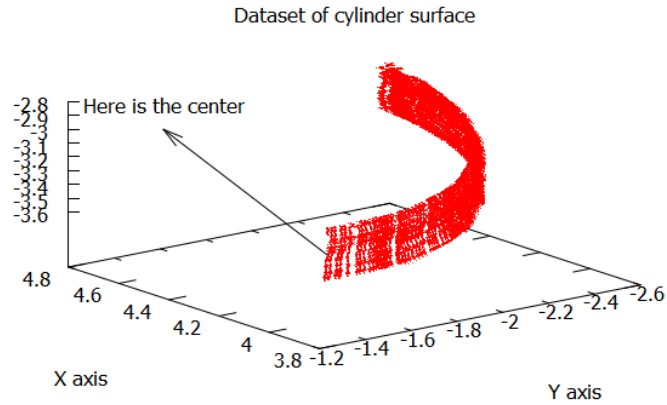


Figure 16. Position of all the spatial points lay on the cylinder surface. The arrow denotes the coordinate of the center.

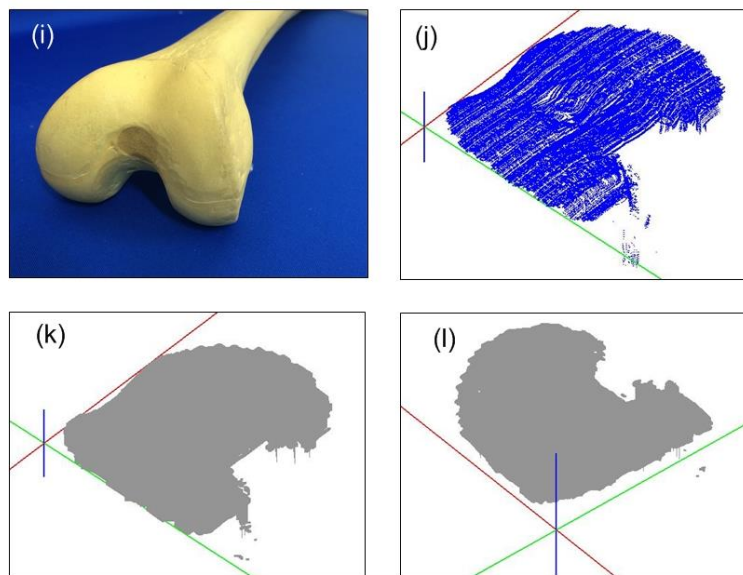


Figure 17. Surface reconstruction of an imitation bone.

4.2. Surface reconstruction

Finally, an imitation bone was used to test the whole effect of reconstruction. Fig. 17(i) is the image of the bone surface. Fig. 17(j) shows the effect of volumetric dataset acquired from the endoscope images. Most of the bone surface details were recovered by the extraction of laser points. Fig. 17(k) and (l) are 3-D reconstruction results in two different viewing angles.

5. Conclusion and discussion

In this paper, we proposed a new system to reconstruct 3-D surface of an object using an endoscope and optical fiber. The surface reconstruction can be achieved in real-time and the average error of the system on depth detection was about 0.5 mm. In addition, a novel marching cube algorithm suitable for endoscope images was proposed to arrange the 3-D grid which is essential for surface extraction in the cubes, and more importantly that the recovered surface can be rendered successfully. The experimental results of the data acquired from endoscope images demonstrated the good performance and feasibility of the proposed method.

Factors affecting the reconstruction accuracy include cube interval and the intensity of the light source attached on the endoscope. The former focuses on the total effect of the recovered surface, while the latter plays a crucial role in accuracy. In our experiments, all of the experiments were carried out without the illumination of light source. Since the inter-

reflection of light [19] on the object surface also can generate the fluctuation while data acquisition.

There are, however, still several limitations in the proposed method. The high accuracy of surface reconstruction is only fit for those objects whose surface are smooth, i.e. featureless objects. Besides, a further limitation is that the look-up table of the proposed method depends only on the complementary symmetry. As a result, it inevitably suffers from a specific problem called the ‘hole problem’, which has been studied in [12], [14], [15] and [17]. Effort in the near future will focus on accuracy improvement of surface recover. One more is to downsize the diameter of endoscope, which is convenient to use for endoscope observation or clinical surgeries.

6. Acknowledgments

This research was partly supported by Grant-in-Aid for Young Scientists (B) from the Ministry of Education, Culture, Science and Technology of Japan under Grant No. 25870273; and also sponsored in part by National Natural Science Foundation of China under Grant No. 51275052; the Key Project Supported by Beijing Natural Science Foundation under Grant No. 3131002. Authors would like to thank Prof. M. Kurosaka, Associ. Prof. R. Kuroda, Dr. T. Matsushita, Dr. Y. Hoshino, and Dr. D. Araki for giving clinical advices.

Reference

- [1] J. Salvi, J. Pages, and J. Batlle, “Pattern codification strategies in structured light systems,” *Pattern Recognition*, vol. 37, no. 4, pp. 827–849, 2004.
- [2] A. Robinson, L. Alboul, and M. Rodrigues, “Methods for indexing stripes in uncoded structured light scanning systems,” 2004.
- [3] S. Chen, Y. F. Li, and J. Zhang, “Vision processing for realtime 3-D data acquisition based on coded structured light,” *IEEE Transactions on Image Processing*, vol. 17, no. 2, pp. 167–176, 2008.
- [4] L. Maier-Hein, P. Mountney, A. Bartoli, H. Elhawary, D. Elson, A. Groch, A. Kolb, M. Rodrigues, J. Sorger, S. Speidel, and others, “Optical techniques for 3D surface reconstruction in computer-assisted laparoscopic surgery,” *Medical image analysis*, vol. 17, no. 8, pp. 974–996, 2013.
- [5] H. Haneishi, T. Ogura, and Y. Miyake, “Profilometry of a gastrointestinal surface by an endoscope with laser beam projection,” *Optics letters*, vol. 19, no. 9, pp. 601–603, 1994.
- [6] K. Hasegawa, K. Noda, and Y. Sato, “Electronic endoscope system for shape measurement,” in *Proceedings of 16th International Conference on Pattern Recognition 2002*, vol. 2, pp. 761–764.
- [7] J.-P. Tardif, S. Roy, and J. Meunier, “Projector-based augmented reality in surgery without calibration,” in *Proceedings of the 25th Annual International Conference of the IEEE Engineering in Medicine and Biology Society, 2003*, vol. 1, pp. 548–551.
- [8] H. Kawasaki, R. Furukawa, R. Sagawa, and Y. Yagi, “Dynamic scene shape reconstruction using a single structured light pattern,” *IEEE Conference on Computer Vision and Pattern Recognition, 2008*, pp. 1–8.
- [9] A. Ben-Hamadou, C. Soussen, C. Daul, W. Blondel, and D. Wolf, “Flexible calibration of structured-light systems projecting point patterns,” *Computer Vision and Image Understanding*, vol. 117, no. 10, pp. 1468–1481, 2013.
- [10] W. E. Lorensen and H. E. Cline, “Marching cubes: A high resolution 3D surface construction algorithm,” in *ACM Siggraph Computer Graphics*, vol. 21, no. 4, pp. 163–169, 1987.
- [11] G. H. Weber, G. Scheuermann, H. Hagen, and B. Hamann, “Exploring scalar fields using critical isovalues,” in *Visualization IEEE, 2002*. pp. 171–178.
- [12] K. Delibasis, G. Matsopoulos, N. Mouravliansky, and K. Nikita, “A novel and efficient implementation of the marching cubes algorithm,” *Computerized Medical Imaging and Graphics*, vol. 25, no. 4, pp. 343–352, 2001.
- [13] B. Golosio, G. L. Masala, and P. Oliva, “A novel multi- threshold method for nodule

- detection in lung CT,” *Medical Physics*, vol. 36, no. 8, pp. 3607–3618, 2009.
- [14] G. L. Masala, B. Golosio, and P. Oliva, “An improved Marching Cube algorithm for 3D data segmentation,” *Computer Physics Communications*, vol. 184, no. 3, pp. 777–782, 2013.
- [15] T. S. Newman and H. Yi, “A survey of the marching cubes algorithm,” *Computers & Graphics*, vol. 30, no. 5, pp. 854–879, 2006.
- [16] Available: http://www.vision.caltech.edu/bouguetj/calib_doc/. [Accessed: 27-Oct-2014]
- [17] C. Montani, R. Scateni, and R. Scopigno, “Discretized marching cubes,” in *Proceedings of the conference on Visualization '94*, 1994, pp. 281–287.
- [18] N. Chernov and C. Lesort, “Least squares fitting of circles,” *Journal of Mathematical Imaging and Vision*, vol. 23, no. 3, pp. 239–252, 2005.
- [19] T. Okatani and K. Deguchi, “Shape reconstruction from an endoscope image by shape from shading technique for a point light source at the projection center,” *Computer vision and image understanding*, vol. 66, no. 2, pp. 119–131, 1997.

*Corresponding author: Kouki Nagamune,
 Department of Human and Artificial Intelligent Systems,
 Graduate School of Engineering, University of Fukui,
 3-9-1 Bunkyo, Fukui 910-8507, Japan.
 E-mail: nagamune@u-fukui.ac.jp

Author Biographies



Name:
 Zhongjie Long

Affiliation:
 Ph.D student, Department of Human and Artificial Intelligent Systems,
 Graduate School of Engineering, University of Fukui

Address:
 3-9-1 Bunkyo, Fukui-shi, Fukui, 910-0017, Japan

Brief Biographical History:
 2013: Received his Master degree of Mechanical Engineering from Beijing Information Science and Technology University, China

Main Works:
 computer-aided surgery, computer-aided diagnosis



Name:
 Kouki Nagamune

Affiliation:
 Associate Professor, Department of Human and Artificial Intelligent Systems, Graduate School of Engineering, University of Fukui

Address:
 3-9-1 Bunkyo, Fukui-shi, Fukui, 910-0017, Japan

Brief Biographical History:
 2004: Received Ph.D degree of Computer Engineering from Himeji Institute of Technology, Japan

Main Works:
 computer-aided surgery, computer-aided diagnosis, signal processing, and fuzzy logic

Membership in Learned Societies:
 The Institute of Electronics, Information and Communication Engineers (IEICE)
 The Institute of Electrical and Electronics Engineers (IEEE)
